SUB-KILOPARSEC IMAGING OF COOL MOLECULAR GAS IN TWO STRONGLY LENSED DUSTY, STAR-FORMING GALAXIES

J. S. SPILKER[1], M. ARAVENA[2], D. P. MARRONE[1], M. BÉTHERMIN[3], M. S. BOTHWELL[4], J. E. CARLSTROM[5,6,7,8], S. C. CHAPMAN[9], J. D. COLLIER[10,11], C. DE BREUCK[3], C. D. FASSNACHT[12], T. GALVIN[10,11], A. H. GONZALEZ[13], J. GONZÁLEZ-LÓPEZ[14], K. GRIEVE[10], Y. HEZAVEH[15], J. MA[13], M. MALKAN[16], A. O'BRIEN[10,11], K. M. ROTERMUND[9], M. STRANDET[17], J. D. VIEIRA[18], A. WEISS[17], AND G. F. WONG[10,11]

[1] Steward Observatory, University of Arizona, 933 North Cherry Avenue, Tucson, AZ 85721, USA; jspilker@as.arizona.edu
[2] Núcleo de Astronomía, Facultad de Ingeniería, Universidad Diego Portales, Av. Ejército 441, Santiago, Chile
[3] European Southern Observatory, Karl Schwarzschild Straße 2, D-85748 Garching, Germany
[4] Cavendish Laboratory, University of Cambridge, JJ Thompson Ave, Cambridge CB3 0HA, UK
[5] Kavli Institute for Cosmological Physics, University of Chicago, 5640 South Ellis Avenue, Chicago, IL 60637, USA
[6] Enrico Fermi Institute, University of Chicago, 5640 South Ellis Avenue, Chicago, IL 60637, USA
[7] Department of Physics, University of Chicago, 5640 South Ellis Avenue, Chicago, IL 60637, USA
[8] Department of Astronomy and Astrophysics, University of Chicago, 5640 South Ellis Avenue, Chicago, IL 60637, USA
[9] Dalhousie University, Halifax, Nova Scotia, Canada
[10] University of Western Sydney, Locked Bag 1797, Penrith, NSW 2751, Australia
[11] CSIRO Astronomy & Space Science, Australia Telescope National Facility, P.O. Box 76, Epping, NSW 2121, Australia
[12] Department of Physics, University of California, One Shields Avenue, Davis, CA 95616, USA
[13] Department of Astronomy, University of Florida, Gainesville, FL 32611, USA
[14] Instituto de Astrofísica, Facultad de Física, Pontificia Universidad Católica de Chile, Av. Vicuña Mackenna 4860, 782-0436 Macul, Santiago, Chile
[15] Kavli Institute for Particle Astrophysics and Cosmology, Stanford University, Stanford, CA 94305, USA
[16] Department of Physics and Astronomy, University of California, Los Angeles, CA 90095-1547, USA
[17] Max-Planck-Institut für Radioastronomie, Auf dem Hügel 69 D-53121 Bonn, Germany
[18] Department of Astronomy and Department of Physics, University of Illinois, 1002 West Green St., Urbana, IL 61801, USA

ABSTRACT

We present spatially resolved imaging obtained with the Australia Telescope Compact Array (ATCA) of three CO lines in two high-redshift gravitationally lensed dusty star-forming galaxies, discovered by the South Pole Telescope. Strong lensing allows us to probe the structure and dynamics of the molecular gas in these two objects, at $z = 2.78$ and $z = 5.66$, with effective source-plane resolution of less than 1 kpc. We model the lensed emission from multiple CO transitions and the dust continuum in a consistent manner, finding that the cold molecular gas as traced by low-J CO always has a larger half-light radius than the 870 μm dust continuum emission. This size difference leads to up to 50% differences in the magnification factor for the cold gas compared to dust. In the $z = 2.78$ galaxy, these CO observations confirm that the background source is undergoing a major merger, while the velocity field of the other source is more complex. We use the ATCA CO observations and comparable resolution Atacama Large Millimeter/submillimeter Array dust continuum imaging of the same objects to constrain the CO–H_2 conversion factor with three different procedures, finding good agreement between the methods and values consistent with those found for rapidly star-forming systems. We discuss these galaxies in the context of the star formation—gas mass surface density relation, noting that the change in emitting area with observed CO transition must be accounted for when comparing high-redshift galaxies to their lower redshift counterparts.

Key words: galaxies: high-redshift – galaxies: ISM – galaxies: star formation – ISM: molecules

1. INTRODUCTION

Carbon monoxide ($^{12}C^{16}O$; hereafter CO) has long been known as a tracer of molecular hydrogen gas in galaxies. Molecular gas is the fuel for new generations of stars (for recent reviews, see Bolatto et al. 2013 and Carilli & Walter 2013), so accurately diagnosing its abundance, kinematics, and morphology can shed light on the astrophysics of star formation (SF). The most intense bouts of SF in the universe appear to occur in dusty, star-forming galaxies (DSFGs) at high redshift (e.g., Casey et al. 2014). These galaxies are heavily enshrouded in dust, which absorbs the ultraviolet radiation from massive young stars and reradiates at far-IR and submillimeter wavelengths. These galaxies lie in contrast to the bulk of the high-redshift galaxy population, which form stars more slowly in less dusty, generally isolated systems (e.g., Förster Schreiber et al. 2009; Daddi et al. 2010; Tacconi

et al. 2013). Such "normal" galaxies are selected by their stellar, rather than dust, emission, which generally excludes the highly obscured DSFG population. Together with rapid SF, DSFGs contain comparably large reservoirs of molecular gas ($>10^{10}$ $M_\odot$; e.g., Greve et al. 2005; Ivison et al. 2011; Bothwell et al. 2013b) that make up a significant fraction ($\sim$20%–80%) of the total baryonic mass (e.g., Carilli et al. 2010; Ivison et al. 2011; Carilli & Walter 2013).

The most extreme DSFGs are likely to be galaxies undergoing major mergers (e.g., Narayanan et al. 2010; Hayward et al. 2012; Fu et al. 2013; Ivison et al. 2013, though see Carilli et al. 2010; Hodge et al. 2012, 2015 for a notable counterexample), with star formation rates (SFRs) enhanced by gas being funneled to the center of the system after being disrupted during the collision. The merger kinematically manifests as a disordered velocity field or multiple components closely separated in position and/or velocity (e.g., Engel et al. 2010;

Fu et al. 2013). Such an extreme level of SF can likely only be sustained for a period of $\lesssim 100$ Myr (Greve et al. 2005), and thus the brightest DSFGs are also relatively rare.

Extensive effort has gone toward studying gas and dust both in the local universe and at high redshift in order to understand the physics and history of SF. One of the most studied correlations is the power-law relationship between the gas surface density, Σ_{gas}, and the SFR surface density, Σ_{SFR} (Schmidt 1959; Kennicutt 1998; see Kennicutt & Evans 2012 for a recent review). On scales of a few 100 pc, the two quantities appear linearly related (e.g., Schruba et al. 2011; Leroy et al. 2013), though power-law exponents ranging from sub-linear to quadratic have also been theoretically predicted and observationally confirmed depending on methodology (e.g., Krumholz et al. 2009; Liu et al. 2011; Faucher-Giguère et al. 2013; Shetty et al. 2013). This SF relation (or Schmidt–Kennicutt relation) is one ingredient in many theoretical prescriptions for SF, so understanding its mathematical form and range of applicability is important for understanding the buildup of stellar mass.

The steps to derive a molecular gas mass from the luminosity of a low-J CO transition are not straightforward, and a variety of techniques have been presented in the literature (e.g., Bolatto et al. 2013). The conversion factor, α_{CO}, varies with the kinematic state of the gas (through the escape fraction of CO photons) and the gas metallicity (through CO formation and destruction processes). A variety of observations suggest that a value of $\alpha_{\text{CO}} \sim 3.6$–4.5 $M_\odot$ pc^{-2}(K km s^{-1})$^{-1}$ (including a 36% mass contribution from the cosmological abundance of helium; hereafter we suppress the units of α_{CO}) is applicable to the Milky Way and nearby quiescently star-forming galaxies with approximately solar metallicity (e.g., Solomon et al. 1987; Abdo et al. 2010; Sandstrom et al. 2013). In regions of vigorous SF, however, α_{CO} decreases by a factor of several (e.g., Downes & Solomon 1998; Tacconi et al. 2008).

As a further complication, the high-Σ_{SFR} galaxies that are much more common at high redshift are rare in the local universe, which makes their exploration more difficult. Due to the faintness of the lowest transitions of CO, most high-redshift studies of molecular gas have used either spatially unresolved observations, or brighter, higher-J transitions with higher excitation conditions than the ground state, or in some cases both. An additional conversion from the observed CO transition to CO(1–0) is required, which depends on the temperature, density, and structure of the interstellar medium (ISM). Resolved observations of the lowest CO transitions are needed to test the SF relation on sub-galactic scales.

Such high-resolution studies are aided by the use of gravitational lensing, in which a background object is magnified by a foreground structure, usually a massive elliptical galaxy or galaxy cluster. For example, Rawle et al. (2014) use high-resolution maps of dust continuum emission and [C II] and CO(1–0) emission to spatially and spectrally decompose a source at $z = 5.2$ predominantly lensed by a $z = 0.63$ galaxy, finding variations in the efficiency of SF of a factor of $\sim 6\times$ within a 4 kpc region in the source plane. Thomson et al. (2015) probe ~ 100 pc scales in the $z = 2.3$ galaxy SMM J2135–0102 ("the Eyelash"; Swinbank et al. 2010). These authors studied the Schmidt–Kennicutt relation in individual star-forming clumps in this galaxy, and found evidence that the clumps are offset toward higher SF efficiency compared to the galaxy as a whole.

Bright lensed galaxies are rare, but recent large surveys conducted by the South Pole Telescope (SPT; Vieira et al. 2010; Carlstrom et al. 2011; Mocanu et al. 2013) and *Herschel* (Negrello et al. 2010; Wardlow et al. 2013) have discovered large numbers of lensed DSFGs. Subsequent spectroscopy and high-resolution imaging have confirmed that the large majority of these objects indeed lie at high redshifts and are lensed (Harris et al. 2012; Bussmann et al. 2013; Hezaveh et al. 2013; Vieira et al. 2013; Weiß et al. 2013). In particular, Weiß et al. (2013) used the Atacama Large Millimeter/submillimeter Array (ALMA) to conduct a redshift survey of 26 DSFGs discovered by the SPT, finding a median redshift $\langle z \rangle = 3.5$. Additionally, M. Aravena et al. (2013, 2015, in preparation) surveyed 18 of these galaxies in low-J CO (either CO(1–0) or CO(2–1)).

In this paper, we present high-resolution observations of low-J CO emission in two DSFGs from the SPT sample performed with the Australia Telescope Compact Array (ATCA). Both objects have been observed at comparable ($\sim 0\rlap{.}''5$) resolution by ALMA at 870 μm, with lens models determined from these data (Hezaveh et al. 2013). SPT-S J053816-5030.8 (SPT0538-50), at $z = 2.78$, is representative of the typical DSFG population in redshift, 870 μm flux density, and dust temperature. This object was studied in detail by Bothwell et al. (2013a), who showed evidence for two velocity components in CO(7–6) separated by $\Delta v \sim 350$ km s^{-1}. Intriguingly, the lens model of this source (Hezaveh et al. 2013) also required two dust components to reproduce the ALMA data, suggesting a possible physical connection between the velocity structure and the continuum structure. SPT-S J034640-5204.9 (SPT0346-52), at $z = 5.66$, is among the highest-redshift DSFGs known. The ALMA lens model indicates that it is also the most intrinsically luminous object in the SPT sample, and its Σ_{SFR} approaches or surpasses the Eddington limit for radiation pressure on dust grains (Thompson et al. 2005). While not representative of the typical DSFG in the SPT sample, SPT0346-52 allows us to study the conditions of the ISM at their most extreme.

The layout of this paper is as follows. In Section 2, we describe the ATCA 7 mm and 3 mm observations of CO lines in these two objects. In Section 3, we describe our procedure for modeling the effects of gravitational lensing in both the ATCA and ALMA data. The morphological and kinematic results of these lens models are given in Section 4. In Section 5, we use the lens modeling results to discuss the effects of preferential source magnification, determine the α_{CO} factor in each source, and place these sources in the context of the SF relation. We conclude in Section 6. We adopt the WMAP9 ΛCDM cosmology, with $(\Omega_m, \Omega_\Lambda, H_0) = (0.286, 0.713, 69.3$ km s^{-1} Mpc^{-1}) (Hinshaw et al. 2013). Throughout, we define the total infrared luminosity, L_{IR}, to be integrated over rest-frame 8–1000 μm, and assume a Chabrier (2003) initial mass function.

2. OBSERVATIONS

Table 1 summarizes the ATCA observations of CO lines in SPT0346-52 and SPT0538-50. Further details of these observations are given below. We also make use of ALMA 870 μm continuum observations of these objects, described further in Hezaveh et al. (2013).

Table 1
Observational Summary

Source	Line	$\nu_{\rm obs}$ (GHz)	Dates	Array Configuration	Time On-source (h)	Beam Size[a]	$\sigma^{\rm b}$ (μJy)
SPT0346-52	CO(2–1)	34.636	2012 10/04–10/09	H 214	5.5	$6''\!.4 \times 4''\!.8$	142
			2014 01/17–01/18	1.5 B	6.0	$1''\!.0 \times 0''\!.6$	180
			2014 05/10–05/17	1.5 D	7.2	$1''\!.6 \times 0''\!.8$	178
			2013 10/23–11/08	6 A	26.1	$0''\!.5 \times 0''\!.3$	66
SPT0538-50	CO(1–0)	30.450	2012 07/28–07/29	H 75	8.5	$19'' \times 13''$	163
			2014 01/18–01/20	1.5 B	11.9	$0''\!.9 \times 0''\!.5$	119
			2014 05/15–05/17	1.5 D	11.3	$1''\!.2 \times 0''\!.6$	96
			2013 10/24–11/08	6 A	45.7	$0''\!.5 \times 0''\!.3$	42
SPT0538-50	CO(3–2)	91.345	2013 08/20	H 168	8.7	$3''\!.1 \times 2''\!.2$	420

Notes.
[a] Beam size for a naturally weighted image.
[b] rms sensitivity in 200 km s^{-1} (SPT0346-52) or 350 km s^{-1} (SPT0538-50) channels.

2.1. ATCA Observations: 7 mm Band

SPT0538-50 and SPT0346-52 were observed with the ATCA 7 mm receivers in CO(1–0) and CO(2–1) at observed frequencies of 30.45 and 34.64 GHz, respectively, as part of project IDs C2892 and C2983. The sources were observed using a 6-km extended array configuration over the course of 12 nights in 2013 October–November and a compact 1.5-km array configuration over 6 nights in 2014 January and May. The two CO lines are redshifted to similar frequencies and can be observed without retuning the two 1 GHz-wide basebands available using the Compact Array Broadband Backend (CABB), allowing bandpass and absolute flux calibration to be shared between the two sources observed in a single track. The bright quasars PKS1921-293 and PKS0537-441 were observed for bandpass calibration, while the quasars PKS0322-403 and PKS0537-441 served as complex gain calibrators for SPT0346-52 and SPT0538-50, respectively. For most tracks, the quasar PKS1934-638 was observed for flux calibration; when this source was not available, the flux level of the bandpass and gain calibrators from adjoining observing dates was used to set the amplitude scale. Repeated observations of amplitude calibration sources indicate that the absolute flux scale is accurate to within 10%.

The two SPT DSFGs were also observed by M. Aravena et al. (2013, 2015, in preparation) using the compact ATCA configurations H75 (SPT0538-50, project C2655) and H214 (SPT0346-52, project C2744) in 2012 July and October, respectively. For our present purposes, the baselines provided by these compact array configurations provide sensitivity to extended emission and an estimate of the total flux. The integrated spectrum of each source derived from these data are shown in Figures 1 and 2. The spectrum of SPT0538-50 has two peaks, as noted by Aravena et al. (2013), which we discuss further in Section 3.

The three array configurations provide good uv coverage on baselines from ∼100 m to 6 km, and were combined and inverted using natural weighting. We ensure proper normalization of the noise levels of each dataset by differencing successive pairs of visibilities on the same baseline and polarization. Naturally weighted channel maps of each galaxy are shown in Figure 1 and the upper panels of Figure 2. We show channel maps of CO(2–1) in SPT0346-52 in 200 km s^{-1} -wide channels, and separate the CO(1–0) line of SPT0538-50 into the red and blue velocity components seen in the integrated spectrum (two channels, approximately 350 km s^{-1} wide). Note that the red velocity component of SPT0538-50 is not significantly detected, as the weak line flux is spread over several synthesized beams. The 1σ sensitivities of these maps are 54 μJy beam^{-1} (170 mK) per 200 km s^{-1} channel in SPT0346-52 and 36 μJy beam^{-1} (53 mK) per 350 km s^{-1} channel in SPT0538-50.

2.2. ATCA Observations: 3 mm Band

For SPT0538-50, we also observed the CO(3–2) line, redshifted to 91.35 GHz, using the hybrid H168 array configuration on 2013 August 20 in project C2816. The other 1 GHz-wide baseband was tuned to 94 GHz. The quasar PKS0537-441 was again used for bandpass and complex gain calibration, while Uranus was observed for flux calibration. The absolute flux scale at 3 mm is expected to be accurate to within ∼15%, again inferred from repeated observations of amplitude calibration sources.

The data were continuum-subtracted and imaged using natural weighting to maximize sensitivity to weak emission, giving a synthesized beam of ∼3.1 × 2$''\!$.2. This resolution is sufficient to marginally resolve the source, as seen in the bottom panels of Figure 2, where we have again imaged the line in each of the two CO velocity peaks separately. These maps reach a sensitivity of 420 μJy beam^{-1} (8.6 mK) in each 350 km s^{-1} channel. Due to the larger synthesized beam size and higher line flux of the CO(3–2) line compared to the CO (1–0) line, we are also able to detect the weak, red velocity component in these data, at ∼6σ significance.

We also significantly detect the dust continuum emission at 3.3 mm using the line-free channels of both basebands, reaching a sensitivity of 90 μJy beam^{-1}. The dust continuum emission closely resembles the emission from the red portion of the CO(3–2) line, which we discuss further in Section 4.2.

3. LENS MODELING

To derive the intrinsic gas and dust properties of the two DSFGs presented here, we must quantify the effects of gravitational lensing. Our lens modeling procedure follows that described by Hezaveh et al. (2013). Briefly, the lens mass profile is represented by a Singular Isothermal Ellipsoid (SIE). For SPT0346-52, the model also strongly favors the existence of an external shear component whose axis is aligned with another galaxy ∼3$''$ east of the primary lens. For both sources, the ALMA 870 μm data are of much higher significance than
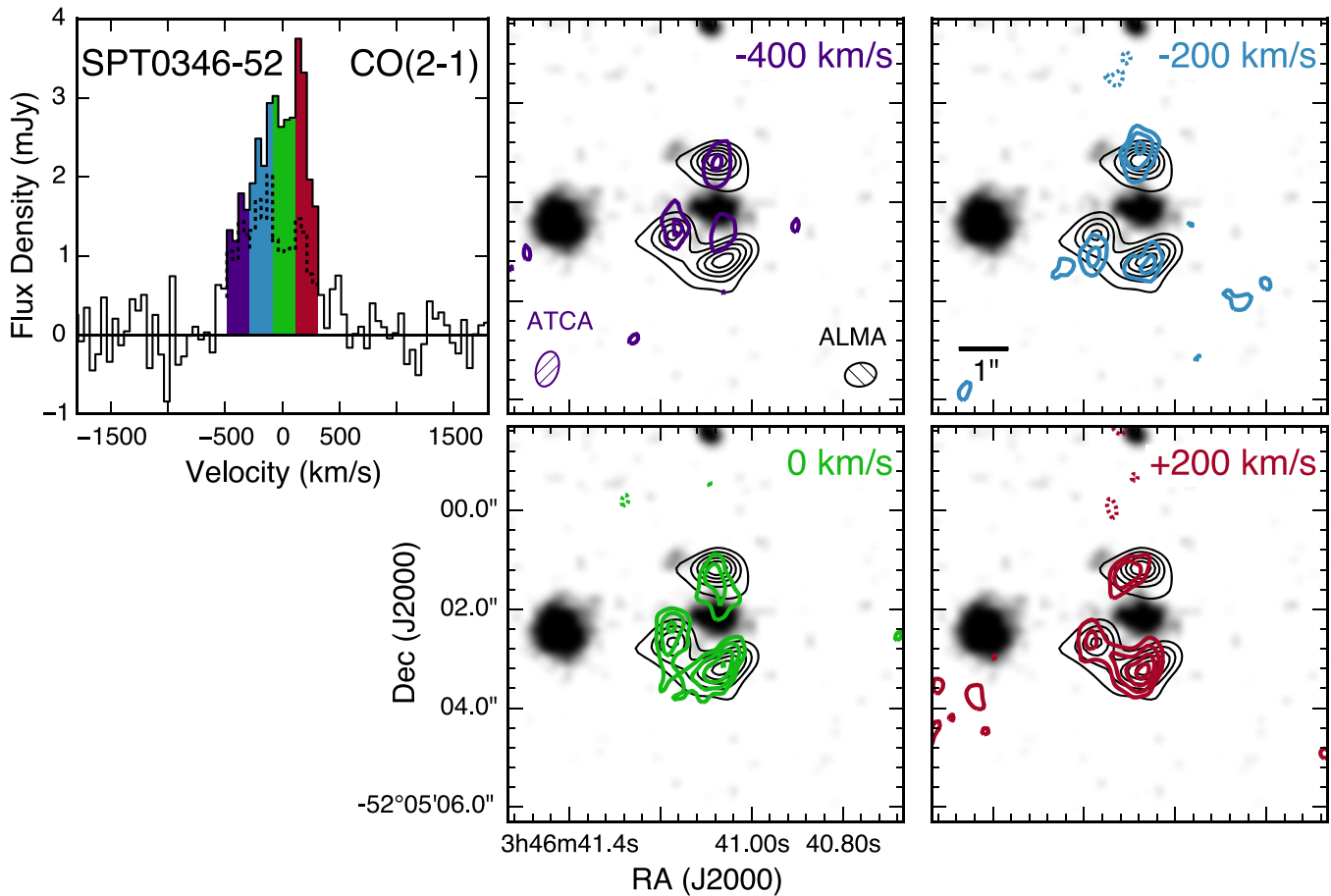
Figure 1. Spectrum and channel maps of CO(2–1) observed in SPT0346-52. *Left*: integrated spectrum derived from short, unresolved baselines, as presented in M. Aravena et al. (2015, in preparation). The four 200 km s^{-1} channels that we model are colored. The dashed line shows the intrinsic spectrum using the magnification factors in Table 2, multiplied by 4× for clarity. *Right panels*: channel maps of the high-resolution ATCA CO(2–1) observations presented here, colored as in the left panel. The grayscale image of the lens galaxy is from co-added *HST*/WFC3 F140W + F160W images (Vieira et al. 2013). Thin black contours show the ALMA 870 μm dust continuum images. The ATCA images are shown in steps of 2σ starting at ±3σ (1σ = 10.6 mJy km s^{-1} beam^{-1}). The ALMA images are shown in steps of 5σ (1σ = 0.80 mJy beam^{-1}). Both data sets reach a resolution of approximately 0″45 × 0″65.

the ATCA observations presented here, so we use the best-fit lens properties derived from the ALMA continuum data to model the source-plane in the ATCA CO data.

The lensed CO source is represented by a parameterized model consisting of one (SPT0346-52) or two (SPT0538-50; see below) symmetric Gaussian light profiles in each modeled velocity channel. Each profile has up to four free parameters, namely, the two-dimensional centroid of the source and its intrinsic flux and size. While this source-plane model is undoubtedly overly simplistic, it allows the derived properties of each velocity bin to be compared in a straightforward manner. Using a parametric model additionally avoids over-fitting the data using a large number of free parameters, as in most pixel-based reconstruction techniques, which are more appropriate for very high resolution, very high signal-to-noise ratio observations.

ATCA and ALMA both measure the Fourier components (visibilities) of the sky at the two-dimensional spatial frequencies defined by pairs of antennas. Rather than comparing to reconstructed images, where there are strong correlations between pixels, we fit lensing models directly to the measured visibilities. As in Hezaveh et al. (2013), we use a Bayesian Markov Chain Monte Carlo (MCMC) fitting procedure. At each MCMC step, we generate a model lensed

image from a given set of source parameters. We then invert this image to the Fourier domain and interpolate the model visibilities to the measured *uv* coordinates of the ATCA data, using the χ^2 metric to determine the quality of the fit.

Lens modeling of the 870 μm dust continuum emission of both sources was previously presented in Hezaveh et al. (2013) using ALMA data with approximately 1″5 resolution. In the present work, we additionally make use of higher resolution data taken as part of the same ALMA program, but which were not yet available at the time of publication of Hezaveh et al. These new data were taken in an extended array configuration available in ALMA Cycle 0, and reach ~0″5 resolution. Further observational details of this ALMA program are given in Hezaveh et al. (2013), while the updated 870 μm lens models will be presented in full in J. Spilker et al. (2015, in preparation). For both sources, the updated lens models using the higher-resolution data are qualitatively and quantitatively similar to those derived by Hezaveh et al. Source properties relevant to this work are summarized in Table 2.

In SPT0346-52, the background source is well-fit by a single elliptical Sérsic light profile with a circularized half-light radius of 610 ± 30 pc. The source's intrinsic 870 μm flux density of 19.6 ± 0.5 mJy is magnified by a factor of μ = 5.5 ± 0.1.
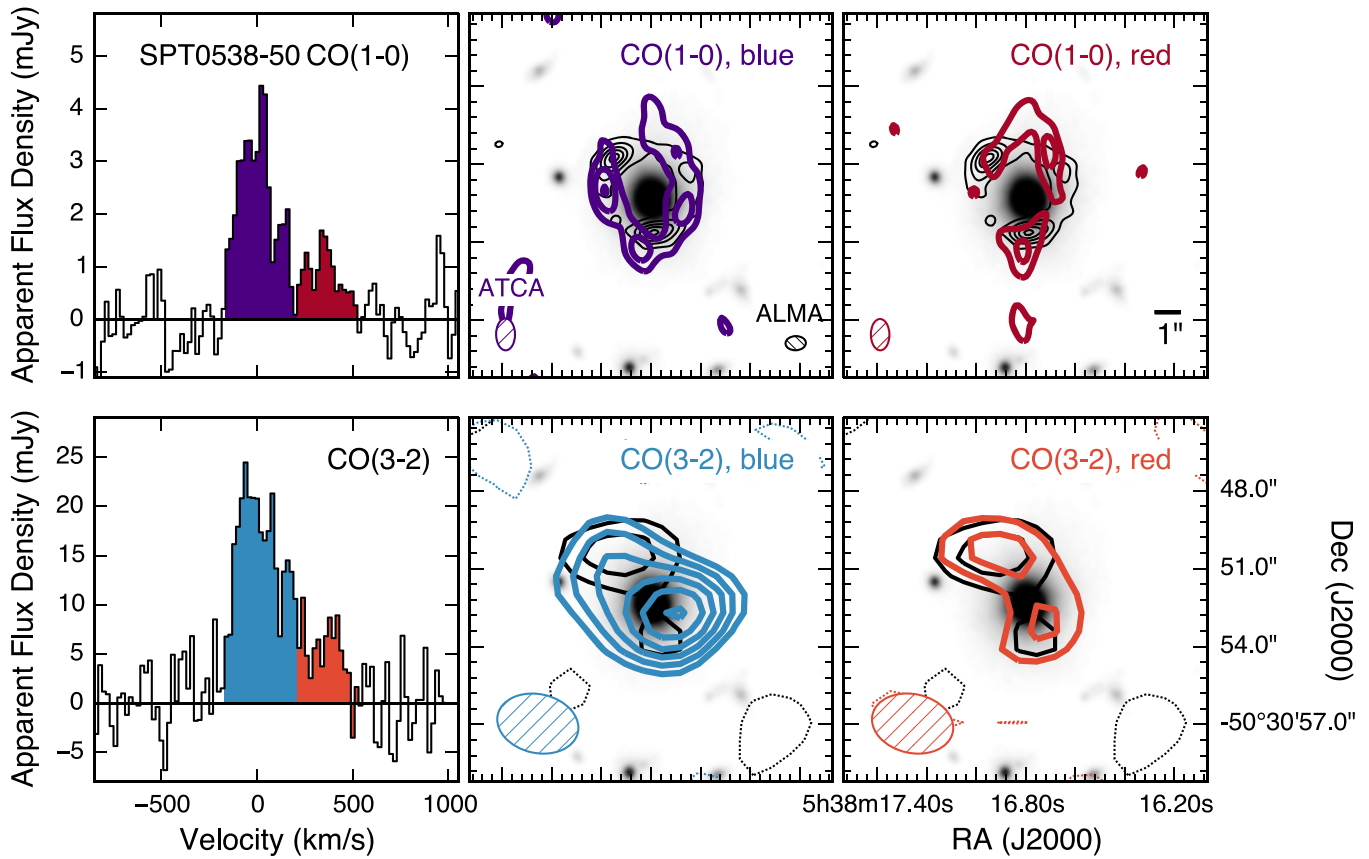
Figure 2. Spectra and channel maps of CO(1–0) and CO(3–2) observed by ATCA in SPT0538-50. Left panels: integrated spectra of each line derived from short baselines in which the source is unresolved. We separate the two velocity components seen in these and other spectral lines as in Bothwell et al. (2013a). Top center and right panels: channel maps of CO(1–0) of each of the colored velocity bins in the top left panel. The grayscale image is a co-added *HST*/WFC3 F140W + F160W image. Also shown as thin black contours are the ALMA 870 μm dust continuum observations. ATCA contours are shown in steps of 2σ, starting at $\pm 3\sigma$ ($1\sigma = 12.7$ mJy km s^{-1} beam^{-1}), with a resolution of approximately $0\rlap{.}''7 \times 1\rlap{.}''2$. The red velocity component is not significantly detected at the depth and resolution of these observations. ALMA contours are shown in steps of 10σ starting at $+5\sigma$ ($1\sigma \sim 0.46$ mJy beam^{-1}). Bottom center and right panels: channel maps of CO(3–2) in each of the colored channels in the lower left panel. Thick black contours show the 3.3 mm continuum emission from the same data. All ATCA contours in these panels are shown in steps of 2σ starting at $\pm 3\sigma$. For the CO(3–2) data, $1\sigma = 145$ mJy km s^{-1} beam^{-1}; for the 3.3 mm continuum data, $1\sigma \sim 70$ μJy beam^{-1}. The ATCA data have a resolution of approximately $2\rlap{.}''2 \times 3\rlap{.}''3$. It is clear from this figure that the red CO(3–2) component is morphologically similar to the dust emission at the same wavelength, dominated by the bright, compact dust component found in the ALMA lens models (see the text).

In SPT0538-50, the updated lens model requires two source-plane components to fit the data, as in Hezaveh et al. The source consists of a faint, diffuse dust component of intrinsic flux density 1.5 ± 0.2 mJy, half-light radius 1.25 ± 0.14 kpc magnified by $\mu = 23.1 \pm 2.2$, and a brighter, more compact component of flux density 3.7 ± 0.4 mJy and half-light radius 470 ± 50 pc magnified by $\mu = 18.9 \pm 2.2$.

4. RESULTS

4.1. SPT0346-52

As shown in Figure 1, we detect the CO(2–1) emission from SPT0346-52 at peak significance of $>5\sigma$ in four consecutive 200 km s^{-1} wide channels. A single symmetric Gaussian source-plane component for each frequency channel is sufficient to model the observed emission with residuals consistent with noise in all cases. The derived source-plane structure is shown in Figure 3, where we have truncated the models of each channel at the half-light radius for clarity. The line emission blueward of ~ -100 km s^{-1} is significantly offset from the redder emission. We have modeled alternative channelizations of the data, with velocity bins ranging from 100 to 400 km s^{-1}, and all channel widths point toward the

same overall structure. Derived source properties are given in Table 2.

The structure seen in Figure 3 is difficult to interpret. At the depth of these data, the velocity structure is not obviously consistent but not clearly inconsistent with large-scale disc rotation or other bulk motion. As we have only modeled four consecutive velocity channels, it is difficult to rule out either ordered or disordered kinematics. Taking the best-fit centroid of each velocity component at face value, the molecular gas in SPT0346-52 appears more consistent with a merging system than with the massive rotating discs seen in normal star-forming galaxies at moderate redshift by, e.g., Förster Schreiber et al. (2009) and Tacconi et al. (2013). If, on the other hand, the centroid of the -200 km s^{-1} component is, in fact, between the bluer and redder channels, a position–velocity curve resembling a rotating disc could result. Similar position–velocity diagrams were found by Riechers et al. (2008) and Deane et al. (2013) in the source-plane structure of lensed quasars at $z = 4.1$ and $z = 2.3$, using data of similar significance to that presented here. These authors interpreted their data as suggestive of rotation. Deeper observations are necessary to draw stronger conclusions about the velocity structure of SPT0346-52, as this would allow lens modeling of narrower velocity bins.

Table 2
CO and Dust Lens Modeling Results

		CO Lens Model Properties				
Source	Line	Component	μ_{CO}	L'_{CO} (10^{10} K km s^{-1} pc^2)	$r_{eff,CO}$ (kpc)	$\log(\Sigma_{gas})$ [a,b] ($M_\odot$ pc^{-2})
SPT0346-52	CO(2–1)	−400 km s^{-1}	5.0 ± 0.6	1.6 ± 0.2	0.70 ± 0.13	3.82 ± 0.32
		−200 km s^{-1}	5.8 ± 0.7	2.3 ± 0.3	1.86 ± 0.28	3.14 ± 0.27
		0 km s^{-1}	10.0 ± 0.1	1.5 ± 0.1	0.77 ± 0.07	3.72 ± 0.26
		+200 km s^{-1}	10.1 ± 0.3	1.4 ± 0.1	0.73 ± 0.09	3.74 ± 0.27
SPT0538-50 B	CO(1–0)	blue	15.7 ± 2.3	1.7 ± 0.3	2.34 ± 0.43	2.86 ± 0.26
SPT0538-50 A		red	⋯	⋯	⋯	⋯
SPT0538-50 B	CO(3–2)	blue	25.7 ± 1.2	0.94 ± 0.13	1.03 ± 0.14	⋯
SPT0538-50 A		red	22.6 ± 1.2	0.51 ± 0.07	0.68 ± 0.12	⋯

		Dust Lens Model Properties				
Source	Component	$\mu_{870\,\mu m}$	$S_{870\,\mu m}$ (mJy)	L_{IR} $10^{12}\,L_\odot$	$r_{eff,\,870\,\mu m}$ (kpc)	$\log(\Sigma_{SFR})$ [b] ($M_\odot$ yr^{-1} kpc^{-2})
SPT0346-52	⋯	5.5 ± 0.1	19.6 ± 0.5	36.3 ± 5.4	0.61 ± 0.03	3.19 ± 0.08
SPT0538-50 A	bright	18.9 ± 2.2	3.7 ± 0.4	3.51 ± 0.50	0.47 ± 0.05	2.40 ± 0.11
SPT0538-50 B	faint	23.1 ± 2.2	1.5 ± 0.2	1.48 ± 0.24	1.25 ± 0.14	1.18 ± 0.12

Note. When modeling the CO emission of both objects, we fix the parameters of the lens to their best-fit values derived from the ALMA data. For SPT0538-50, we also fix the location of the A and B source components to the positions derived from the ALMA data.
[a] Assuming the average CO–H_2 conversion factors determined in Section 5.2, 1.4 for SPT0346-52 and 1.5 for SPT0538-50. We propagate an uncertainty of 50% into the determinations of Σ_{gas}.
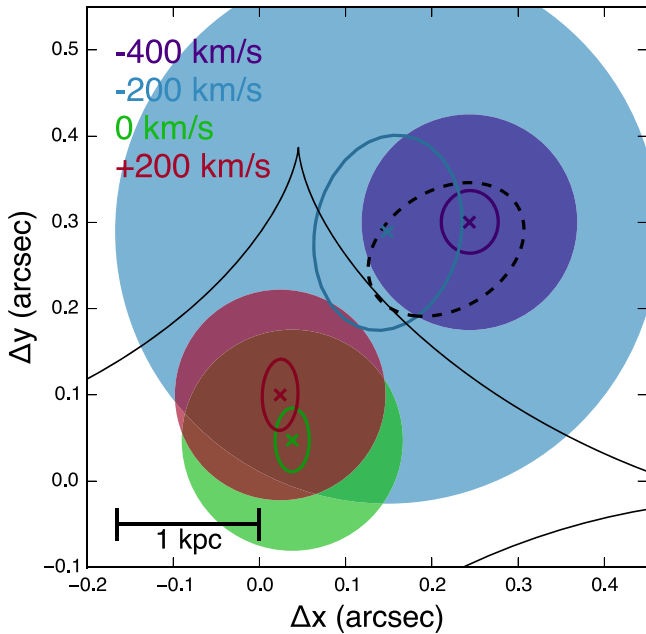[b] Surface densities determined within r_{eff}.

Figure 3. Source-plane reconstruction of SPT0346-52. Each CO(2–1) velocity channel modeled is represented by a colored disk, truncated at the half-light radius. Colored "×" symbols and ellipses show the centroid and 1σ positional uncertainty on the centroid for each channel. The FWHM and location of the 870 μm dust emission is shown as a thick dashed line, while the lensing caustic is shown as a thin black line.

The half-light radius of the background source is larger in low-J CO emission than in rest-frame 130 μm continuum emission, and the 130 μm emission appears closely associated with the blue half of the CO(2–1) emission. This tentatively suggests that the SF in SPT0346-52 is proceeding in a compact region embedded within a larger reservoir of molecular gas. Alternatively, the CO(2–1) emission may trace

a larger region of the galaxy owing to its higher optical depth. To test the degree to which a source with the same size and location as either of the CO-emitting components at 0 and +200 km s^{-1} could contribute to the 130 μm continuum emission, we re-fit the ALMA data with two source-plane components. We fix the size and position of each source, leaving only the flux density of each source as a free parameter. The size and position of one source is fixed to that derived from the ALMA data, while the other is fixed to the size and position of either of the two red CO channels. This is effectively a null test to determine how much flux density at rest 130 μm could be emitted from the same region as the 0 or +200 km s^{-1} CO emission. This test indicates that a source co-located with either of the two reddest modeled CO channels contributes <3% (1σ upper limit) of the total unlensed flux at 130 μm. This is also the fraction of L_{IR} and, by proxy, SFR, that could arise from these locations under the assumptions of a uniform dust temperature across the source and no contribution from dust heating due to active galactic nucleus (AGN) activity. This limit is nevertheless consistent with CO/L_{IR} ratios seen in local ULIRGs and $z > 0.4$ main-sequence galaxies (e.g., Ivison et al. 2011; M. Aravena et al. 2015, in preparation).

We note that our finding of a large CO spatial extent compared to dust continuum is unlikely to be explained by the effects of interferometric filtering. While only a limited range of spatial frequencies are probed by both the ATCA and ALMA data, the data probe a similar range of radii in the uv plane. Additionally, as we fit directly to the visibilities, our model natively reproduces this filtering. The models presented here recover 85%–105% of the flux observed in the most compact array configuration data. These data are included in the modeling, so it is unsurprising that the total flux should be recovered well.

4.2. SPT0538-50

The integrated spectrum of this source shows two velocity components in CO(1–0) emission separated by $\sim$350 km s^{-1} (Figure 2; Aravena et al. 2013; Bothwell et al. 2013a), and so we model the emission from each velocity component separately. Unfortunately, our high-resolution CO(1–0) maps are too shallow to detect the faint red velocity component. However, this source was also observed in CO(3–2) emission, marginally resolving the source and significantly detecting both velocity components. These observations also detected the observed-frame 3.3 mm continuum emission at $\gtrsim 5\sigma$. Here, we discuss the results of the lensing inversion of these three data sets in turn. As before, we fix the parameters of the lens to those derived from the ALMA 870 μm data.

4.2.1. Dust Continuum Emission

As previously described and as found by Hezaveh et al. (2013), we require two source-plane components to fit the 870 μm continuum emission observed by ALMA (rest-frame 230 μm). The source consists of a faint, diffuse dust component of intrinsic flux density 1.4 ± 0.4 mJy, half-light radius 1.2 ± 0.3 kpc magnified by $\mu = 24 \pm 4.5$, and a brighter, more compact component of flux density 3.5 ± 0.7 mJy and half-light radius 460 ± 90 pc magnified by $\mu = 20 \pm 4$.

We have now also detected dust continuum emission at observed-frame 3.3 mm (rest-frame 870 μm) in the line-free channels of our ATCA 3 mm data. As the continuum is much more weakly detected in the ATCA data than the ALMA data (Figure 2), and as dust gives rise to the observed emission at both wavelengths, we fit the ATCA data with two source-plane components with positions and sizes fixed to the best-fit values derived from the ALMA data. This leaves only the fluxes of each component as free parameters.

Assuming the source-plane morphology of the dust emission is the same at both rest-frame 230 and 870 μm, we derive intrinsic fluxes of $55 \pm 15 \mu$Jy for the bright, compact (A) component and $5 \pm 9 \mu$Jy for the faint, diffuse (B) component. By calculating the flux ratio of the components at each MCMC step, we rule out the possibility that the two components have the same 2.5:1 flux ratio seen at 870 μm at the $\sim$2.2σ level, tentative evidence that the two components have different metallicities, dust temperatures and/or opacities. (e.g., Greve & Vieira 2012). Further multi-wavelength high-resolution continuum observations could resolve this issue, though the atmosphere limits such prospects at wavelengths shorter than observed-frame 350 μm (rest-frame 92 μm).

4.2.2. CO(3–2) Emission

In star-forming galaxies, the CO(3–2) transition is significantly more luminous than lower-lying transitions; for thermalized level populations, the integrated line flux scales as J^2. This, combined with the larger beam size of our ATCA 3 mm observations, allowed us to detect the fainter red velocity component in CO(3–2) emission while this component remained undetected in CO(1–0).

As clearly seen in the images of Figure 2, the spatial distributions of the blue and red CO(3–2) emission appear significantly different. The red velocity component appears similar to the rest-frame 870 μm continuum emission simultaneously observed by ATCA. This emission is dominated by the bright, compact (A) dust component, as described in the

previous section. We begin exploring the lensing inversion by fitting a single Gaussian profile to each velocity component, allowing the position, size, and flux of each source to vary. The best-fit position of the blue velocity component is within the 1σ uncertainties of the location of the diffuse B dust component seen in the ALMA data, and inconsistent with the location of the compact A component. While the positional uncertainties are large ($\sim 0\overset{''}{.}13$), the best-fit position of the red velocity component is consistent with the location of the bright, compact dust component seen in the ALMA maps. This suggests that the two velocity components are in fact associated with the two dust components.

Motivated by this association, we re-fit the CO(3–2) data of both the red and blue velocity components with *two* source-plane components each, fixing the positions of each component to the best-fit positions of the dust components in the continuum lens model, allowing the source size to remain a free parameter. This is a test to determine whether the CO emission of each velocity component can be uniquely associated with one of the two dust components. The results of this test strengthen the hypothesis that each velocity component is associated with only one of the two dust components—for each velocity component, the lens modeling prefers that only one of the two source-plane components have positive flux and non-infinite size. Again, we find that the brighter blue velocity component is associated with the faint, diffuse (B) dust component, and the fainter red velocity component is associated with the bright, compact (A) dust component.

Figure 4 shows the results of modeling the CO(3–2) emission, where we have fixed the locations of the blue and red velocity components to the locations of the faint and bright dust components, respectively. For each velocity channel, we allow the flux and size of the modeled source-plane component to vary. The models imply that the CO(3–2)-emitting molecular gas has approximately the same extent as the dust emission in both components.

Having associated the two dust components seen in the lensing reconstruction with the two separate velocity components seen in the integrated CO line spectra, we strengthen the argument that SPT0538-50 is indeed a pair of merging galaxies, as also posited by Bothwell et al. (2013a). Their arguments, based on the high SFR surface density, high specific SFR, and suppressed fine structure lines of SPT0538-50, are confirmed based on our high-resolution kinematic observations. The two merging galaxies are separated by 1.3 kpc in projection and $\sim$375 km s^{-1} in velocity. This is comparable to what is seen in the local ULIRG Arp220, a late-stage merger which shows two nuclei separated by approximately 400 pc and $\sim$250 km s^{-1} (e.g., Scoville et al. 1997; Sakamoto et al. 2009). In contrast, SPT0538-50 appears to be in a more compact merger than the $z = 5.24$ *Herschel*-selected lensed galaxy HLS0918 studied by Rawle et al. (2014), which consists of four spectral components separated by 4 kpc and $\sim$840 km s^{-1}. SPT0538-50 appears to conform with the idea that most DSFGs reach their extreme SFRs through major merger activity (e.g., Engel et al. 2010).

4.3. CO(1–0) Emission

As seen in Figure 2, our observations of CO(1–0) are insufficiently deep to detect the faint, red velocity component in our high-resolution imaging data. We do, however, clearly
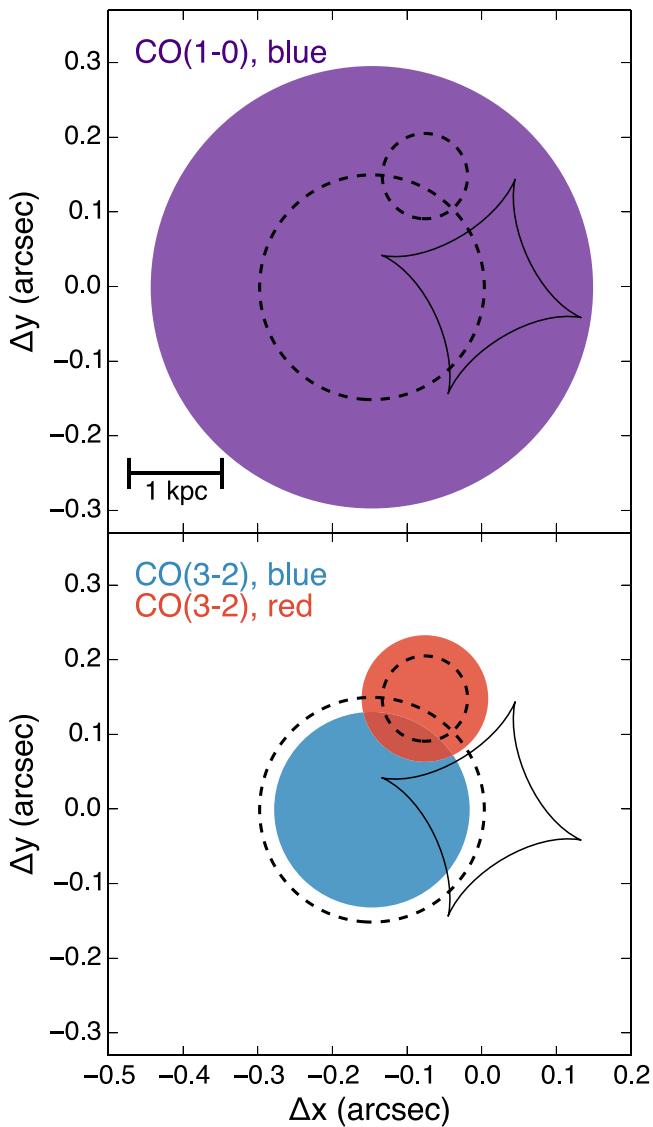
Figure 4. Source-plane reconstruction of SPT0538-50. As before, each component is truncated at its FWHM. In both panels, the bright/compact and faint/extended rest-frame 230 μm dust components are represented by small and large dashed circles. The best-fit extent of the blue CO(1–0) velocity component is shown in the top panel, while the bottom shows the extent of both the blue and red CO(3–2) velocity components. Note that we are unable to model the red CO(1–0) velocity component, and that the centroids of each CO component were fixed to the best-fit positions derived from the ALMA continuum data.

consistent with noise. Comparison of the CO(3–2) and CO (1–0) intrinsic line fluxes implies a CO brightness temperature ratio of $r_{31} \sim 0.6$, similar to the ratios determined for other high-redshift DSFGs and slightly lower than the average ratio for the SPT DSFGs themselves (e.g., Danielson et al. 2011; Bothwell et al. 2013b; Spilker et al. 2014). Similar to what was seen in CO(2–1) in SPT0346-52, we find that the CO(1–0) emission in SPT0538-50 is significantly extended compared to the dust emission. Again, this may indicate that the SF in this system is proceeding in a compact region embedded in a larger reservoir of molecular gas. We return to this discussion in the next section.

5. DISCUSSION

5.1. Source Sizes and Differential Magnification

As can be seen in Figures 3 and 4, we find that the molecular gas reservoirs traced by low-J CO transitions have larger half-light radii than the emission from the dust continuum. If we attribute all of the dust emission to SF (as opposed to, for example, dust heated by AGN activity), this implies that the intense SF in these galaxies is limited to relatively small regions embedded in much larger reservoirs of molecular gas. The kinematics of both galaxies are plausibly consistent with the disruption of secular rotation, causing vast amounts of molecular gas to fall toward dense, compact star-forming regions.

In SPT0538-50, we find that the CO(1–0) is similarly extended compared to CO(3–2), by more than a factor of $2\times$ in the blue velocity component. Size differences of this level were reported by Riechers et al. (2011), comparing the and CO(1–0) sizes of the lensed DSFG SMM J09431+4700. Larger physical extents for low-J CO emission were also inferred by those authors and Ivison et al. (2011) by comparing the CO line widths between low- and mid-J CO transitions. In contrast with the CO(1–0) emission, we find the CO(3–2) emission in SPT0538-50 to have roughly equal half-light radius as the SF traced by the dust continuum. This can be taken as evidence that the CO(3–2) emission is more directly associated with ongoing SF in this galaxy, in agreement with studies both locally (e.g., Wilson et al. 2009) and at high-redshift (Bothwell et al. 2010; Tacconi et al. 2013), which find an approximately linear relationship between the CO(3–2) luminosity and SFR. Indeed, high gas excitation conditions ($T_{\rm kin} \sim 50$ K, $n_{\rm H_2} \sim 1000$ cm^{-3}) are needed to achieve brightness temperature ratios near unity. A similarity in size between CO(3–2) and stellar light was also seen by Tacconi et al. (2013), who used rest-frame B-band *HST* images to determine the extent of the SF in a large sample of $z \sim 1-2$ normal star-forming galaxies.

While measurements are few, in Figure 5 we plot the half-light radii of SF (traced by the rest-frame UV, dust continuum emission, or both) and molecular gas reservoirs for local and high-redshift sources. We restrict this comparison to those galaxies with measured sizes in CO transitions with $J_{\rm up} < 3$, since the effective source size changes significantly as a function of observed transition. Physically large molecular gas reservoirs are common, with an average SF area filling factor of $\sim$55%, similar to the difference in size between gas and SF in local galaxies seen by Bigiel & Blitz (2012) and Zahid et al. (2014). This difference in size can be a potential source of bias when calculating surface-density quantities using sizes derived at different wavelengths—for example, using the source sizes
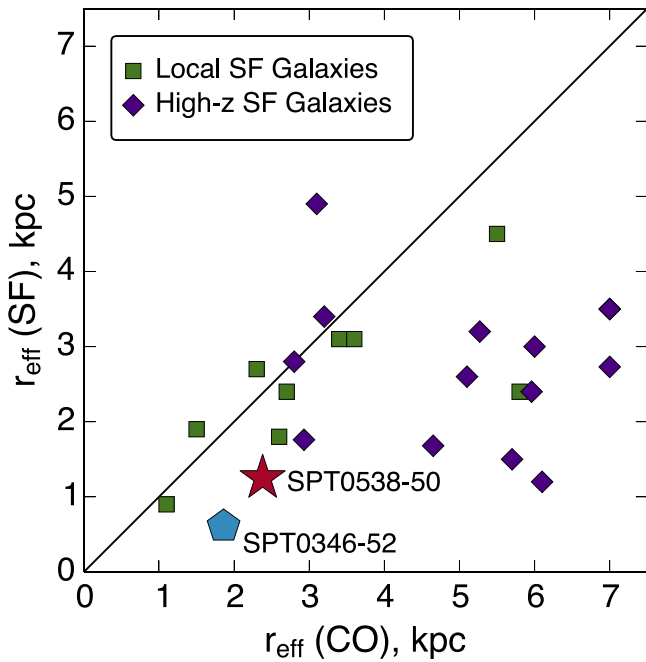
detect the brighter blue velocity component at comparable resolution to the ALMA 870 μm data. The morphology of the CO(1–0) emission is clearly different from that of the dust continuum emission, which is dominated by the bright, compact dust component described previously. While we cannot model the red line component in CO(1–0), we proceed by discussing the blue line component, which can be modeled.

Having established in the previous section that the blue line component is spatially associated with the faint, diffuse dust component, we model the blue CO(1–0) emission with a circularly symmetric Gaussian source-plane component with position fixed to that derived from the ALMA continuum data. The free parameters are the source flux and size, as in our models of the CO(3–2) emission. The best-fit model source, shown in Figure 4 and described in Table 2, leaves residuals

Figure 5. Relative sizes of star formation and molecular gas in galaxies. CO source sizes are confined to those objects for which low-J resolved measurements have been made. Star formation sizes are derived either from rest-frame UV measurements, dust continuum emission, or both. The solid line indicates $r_{\rm eff}({\rm SF}) = r_{\rm eff}({\rm CO})$. The high-redshift sample is drawn from Younger et al. (2008), Daddi et al. (2010), Ivison et al. (2011, 2013), Fu et al. (2012, 2013), Hodge et al. (2012), Walter et al. (2012). The local galaxies are drawn from Regan et al. (2001) and Leroy et al. (2008), where we have scaled the CO sizes in Regan et al. to match the distances in Leroy et al.

Figure 6. Summary of constraints on the CO–H$_2$ conversion factor at $z > 1$ from the literature. Objects are color-coded by the method used to constrain $\alpha_{\rm CO}$ and shape-coded by type of object. SPT0346-52 and SPT0538-50 both appear to follow the general trend of decreasing $\alpha_{\rm CO}$ with increasing $L_{\rm IR}$. Where applicable, $L_{\rm IR}$ has been corrected for lensing magnification. If not given in the original references, measurement uncertainties for the literature objects are shown as 50%. Objects with constraints from multiple methods are shown multiple times at the same $L_{\rm IR}$. Literature objects are compiled from Daddi et al. (2010), Ivison et al. (2011, 2013), Magdis et al. (2011, 2012), Swinbank et al. (2011), Fu et al. (2012, 2013), Hodge et al. (2012, 2013), Magnelli et al. (2012), Walter et al. (2012), Deane et al. (2013), and Messias et al. (2014).

determined from a SF tracer to calculate $\Sigma_{\rm gas}$ would lead to an over-estimation of the *average* surface density by a factor of 80%.

This difference in source size and structure at different emitting wavelengths leads to differential magnification. Although gravitational lensing is achromatic, galaxies appear morphologically different at different wavelengths, leading to wavelength-dependent variations in the lensing magnification (e.g., Blain et al. 1999; Hezaveh et al. 2012; Serjeant 2012). In both sources studied here, the large total extent of the CO emission relative to the dust continuum emission and the proximity of the sources to the lensing caustics lead to differences in magnification between dust and molecular gas of up to ~50%. In SPT0346-52, our data indicate that the gas emitting at positive systemic velocities is magnified by approximately a factor of 2× more than either the rest-frame 130 μm continuum or the gas at bluer systemic velocities. Such a magnification gradient may in fact be a common feature of observing lensed galaxies in spectral lines in which galaxies are expected to have large physical extents. Riechers et al. (2008) and Deane et al. (2013) both find similar levels of differential magnification as a function of velocity in observations of low-J CO emission in the lensed quasars PSS J2322+1944 and IRAS F10214+4724, respectively. These results indicate that differential magnification can cause significant distortion of the global spectral energy distributions (SEDs) of lensed galaxies, reaffirming the need to account for its effects when comparing lensed and unlensed sources.
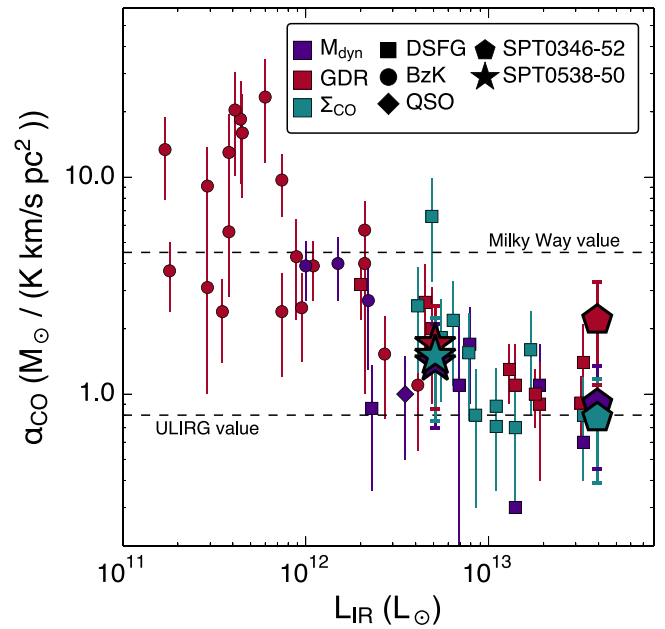
5.2. The CO–H$_2$ Conversion Factor

With the wealth of high-resolution data on these two sources, we are presented with the opportunity to constrain the conversion factor between CO luminosity and molecular gas mass, $\alpha_{\rm CO}$, through multiple means. This allows us to measure the extent to which different methods of determining $\alpha_{\rm CO}$ are consistent within a single system. Below, we briefly describe each technique as applied to SPT0346-52 and SPT0538-50. In each case, we assume the mass in the form of atomic hydrogen gas is negligible, as seems appropriate for dense, highly star-forming systems. We also assume that the CO(2–1) line observed in SPT0346-52 is thermalized and optically thick, with $L'_{\rm CO(1-0)} = L'_{\rm CO(2-1)}$. Given the vigorous SF proceeding in this warm, dense system and that $T_{\rm CMB}(z = 5.7) = 18\,{\rm K} > E_{\rm up,CO(2-1)}/k_B$, this assumption is justified. This ratio is also justified both observationally (see, e.g., Figure 45 of Casey et al. 2014) and theoretically (Narayanan & Krumholz 2014). The results of this section are summarized in Figure 6.

5.2.1. Gas-to-dust Ratio

Gas and dust are widely observed to be well-mixed in galaxies, with dust comprising approximately 1% of the mass in the ISM (e.g., Sandstrom et al. 2013; Draine et al. 2014). Thus, if the mass in dust ($M_{\rm d}$) and the gas-to-dust ratio ($\delta_{\rm GDR}$) can be estimated, $\alpha_{\rm CO}$ can be determined simply as $M_{\rm d}\,\delta_{\rm GDR}/L'_{\rm CO}$.

Extensive *Spitzer* and *Herschel* observations of the dust continuum emission in galaxies have rapidly advanced our understanding of $\delta_{\rm GDR}$ and the nature of the dust emission. The metallicity of the ISM affects $\delta_{\rm GDR}$ so that low-metallicity systems have more gas per unit dust mass. Meanwhile, most far-infrared dust SEDs can be accurately modeled using only a small number of free parameters. One common method is to fit the dust SED with a single-temperature modified blackbody function. However, such single-temperature models generally underestimate the dust mass in galaxies by a factor of $\sim 2\times$ (Dunne & Eales 2001; Dale et al. 2012). Dust at a single temperature cannot simultaneously fit both the long- and short-wavelength sides of the SED, which has contributions from dust heated to a range of equilibrium temperatures. This effect has been explored by Dunne et al. (2000) and Dale et al. (2012), and indicates that a more sophisticated, multi-component approach is needed. Such approaches have been developed by, e.g., Draine & Li (2007) and da Cunha et al. (2008). The theoretical models of Draine & Li (2007) assume the dust is exposed to a power-law distribution of starlight intensities, while the MAGPHYS code of da Cunha et al. (2008) decomposes the dust emission into different physically motivated temperature regimes. The Draine & Li (2007) models have been used to constrain $\alpha_{\rm CO}$ in samples of normal and intensely star-forming $z \sim 0.5-4$ *Herschel*-selected star-forming galaxies observed by Magdis et al. (2012) and Magnelli et al. (2012).

Calculation of the dust mass requires knowledge of the dust mass absorption coefficient, defined here as $\kappa_{870\,\mu\rm m}$, the value of the coefficient at rest-wavelength $870\,\mu\rm m$, in units of $\rm m^2\,kg^{-1}$. The dust mass scales as $\kappa_{870\,\mu\rm m}^{-1}$. Most estimates of $\kappa_{870\,\mu\rm m}$ for dust in nearby, Milky Way-like galaxies are close to either 0.045 (Li & Draine 2001; Draine & Li 2007; Scoville et al. 2014) or 0.075 (Ossenkopf & Henning 1994; Dunne et al. 2000; James et al. 2002). The choice of dust opacity, then, leads to a difference in dust mass of $\sim 70\%$. In this work, we adopt the dust models implemented in MAGPHYS (da Cunha et al. 2008), which uses the dust opacity coefficient of Dunne et al. (2000), $\kappa_{870\,\mu\rm m} = 0.077$. This value for the mass absorption coefficient is commonly used for other high-redshift rapidly star-forming systems.

Finally, to calculate the total gas mass from the dust mass, we require knowledge of the gas-to-dust ratio, $\delta_{\rm GDR}$, which is known to vary with metallicity. As we have essentially no constraints on the metallicities of these systems, we adopt the average $\delta_{\rm GDR}$ determined by Sandstrom et al. (2013) in a large sample of local star-forming galaxies with approximately solar metallicities, $\delta_{\rm GDR} = 72$ with ~ 0.2 dex scatter. We note that the derived $\alpha_{\rm CO}$ conversion factors are linearly proportional to the assumed $\delta_{\rm GDR}$, and $\delta_{\rm GDR}$ itself likely varies approximately linearly with metallicity (Leroy et al. 2011).

We determine the dust masses of SPT0346-52 and SPT0538-50 by fitting to the photometry given in Weiß et al. (2013) and Bothwell et al. (2013a), respectively. In both cases, we assume that differential magnification of the dust emission is insignificant, and for SPT0538-50, we assume the flux at each wavelength is divided between the two components in the same ratio as at rest-frame $230\,\mu\rm m$. This yields dust masses of $2.1 \pm 0.3 \times 10^9\,M_\odot$ for SPT0346-52 and 9.0 ± 1.3 and $3.7 \pm 0.6 \times 10^8\,M_\odot$ for the compact and diffuse components of SPT0538-50, where the uncertainties are statistical only. For SPT0346-52, this dust mass and the source size derived from the ALMA lens model imply that the dust reaches unit optical

depth by rest-frame $\sim 300\,\mu\rm m$, longer than the canonical wavelength of $\sim 100\,\mu\rm m$. Lower optical depths are possible by raising the dust temperature or effective source size. The prevalence of this effect in samples of lensed DSFGs will be explored in more detail by J. Spilker et al. (2015, in preparation).

Using our adopted $\delta_{\rm GDR}$ and dividing by the sum of the intrinsic CO luminosities of each channel yields a measurement of $\alpha_{\rm CO} = 2.2 \pm 0.6$ for SPT0346-52. For SPT0538-50, we calculate $\alpha_{\rm CO}$ for the blue velocity component only, yielding $\alpha_{\rm CO} = 1.7 \pm 0.4$. Note that the uncertainties in these calculations account only for the statistical errors in the dust SED fitting and lens modeling procedure, and neglect systematic uncertainties in $\kappa_{870\,\mu\rm m}$ and $\delta_{\rm GDR}$, which are of order 100%.

5.2.2. Dynamical Constraints

The CO–H$_2$ conversion factor can also be constrained using estimates of the total dynamical mass of galaxies and a process of elimination—the molecular gas mass is the remainder after all other contributions to the dynamical mass have been subtracted (e.g., stars, dark matter, HI gas, dust, etc.). Assuming that stars, molecular gas, and dark matter make up the vast majority of the total mass, then, we have

$$M_{\rm dyn} = M_* + \alpha_{\rm CO} L'_{\rm CO} + M_{\rm DM}, \quad (1)$$

where each of these quantities is measured within the same effective radius defined by the extent of the CO emission.

Measuring each of these quantities is fraught with assumptions and systematic uncertainties. The stellar mass of SPT0538-50 has been estimated by Bothwell et al. (2013a) as $3.3 \pm 1.5 \times 10^{10}\,M_\odot$, while Ma et al. (2015) only place an upper limit on the stellar mass of SPT0346-52, based on SED fitting to optical through far-infrared photometry. These estimates assume the stellar light is magnified by the same factor as the dust emission, which may be inaccurate by up to a factor of $\sim 50\%$ (see Section 5.1 above and Calanog et al. 2014). The dark matter content within the region traced by CO is highly uncertain, but we adopt a contribution of 25% for consistency with the literature (Daddi et al. 2010), based on observations of $z \sim 1.5-2$ disk galaxies.

A crude estimate of the dynamical mass can be derived from

$$M_{\rm dyn} = \gamma R \Delta V^2 / G, \quad (2)$$

with ΔV as the FWHM line width, R as the source effective radius, and the gravitational constant G. Here the pre-factor γ accounts for the detailed geometry of the source, and is of order unity. As the geometry of the two objects studied here is only somewhat constrained, we adopt $\gamma = 1$ for simplicity. Literature values of γ range from $\gamma \sim 0.3$ (e.g., Neri et al. 2003; Tacconi et al. 2008; Daddi et al. 2010) to $\gamma = 1.2$ (e.g., Bothwell et al. 2013b). In the following, we quote only statistical uncertainties on the derived values of $\alpha_{\rm CO}$, ignoring the much larger systematic uncertainties on the stellar mass, dark matter fraction, and true source geometry.

For SPT0538-50, using the spatial separation of the two components of $1.35 \pm 0.16\,\rm kpc$ and a line width of $490\,\rm km\,s^{-1}$ (from the full line profile), the above equation yields $M_{\rm dyn} \sim 7.5 \pm 0.9 \times 10^{10}\,M_\odot$. Combined with the stellar mass estimate given above and a 25% dark matter fraction, this yields $\alpha_{\rm CO} = 1.4 \pm 0.8$. If the stellar mass is entirely concentrated in the blue velocity component, the

implied gas fraction of the blue component is $f_{gas} = M_{gas}/(M_{gas} + M_{star}) \sim 40\%$. As the red component must also contain some gas, 40% is a lower limit to the gas fraction of the entire system.

We estimate the dynamical mass of SPT0346-52 using the separation in space and velocity of the emission at -400 and $+200$ km s^{-1}. This yields $R = 1.8 \pm 0.2$ kpc and $M_{dyn} = 1.5 \pm 0.2 \times 10^{11}\ M_{\odot}$. The stellar mass upper limit calculated by Ma et al. (2015) is a factor of several higher than the dynamical mass we have estimated. To constrain α_{CO}, we instead assume a range of gas fractions of $f_{gas} = 0.3–0.8$. This range has been observed by Tacconi et al. (2013) at lower redshifts ($z \sim 1–2$), and appears to evolve slowly with redshift at $z > 2$ (e.g., Bothwell et al. 2013b; M. Aravena et al. 2015, in preparation). This range in gas fraction leads to a range of $\alpha_{CO} = 0.5–1.3$; we adopt $\alpha_{CO} = 0.9 \pm 0.5$, where the uncertainty reflects only the range of f_{gas} and the statistical uncertainty on M_{dyn}.

Given the large systematic uncertainties inherent in each step of these calculations, we estimate that the uncertainty in these derived conversion factors is at least a factor of $2\times$. Improving these estimates would require extensive high resolution multi-wavelength observations in order to better constrain the dynamical and stellar masses. Refined estimates of the dark matter contribution would be even more challenging, and the best option may simply be to use the dark matter content derived from hydrodynamical simulations of galaxies.

5.2.3. CO Luminosity Surface Density

A third estimator of the CO–H$_2$ conversion factor was developed by Narayanan et al. (2012), based on hydrodynamical simulations coupled with dust and line radiative transfer. Those authors developed a suite of simulated galaxies in isolated and merging systems and provided a fitting formula to α_{CO} that depends solely on the CO line intensity and metallicity:

$$\alpha_{CO} = 10.7 \times \Sigma_{CO}^{-0.32} / (Z/Z_{\odot})^{0.65}, \qquad (3)$$

where Σ_{CO} is the CO luminosity surface density in units of K km s^{-1}. As in the dust-to-gas ratio method, we again assume solar metallicity for both DSFGs considered here; lowering the metallicity to half solar would increase these estimates by approximately 50%. For SPT0346-52, we average the values of α_{CO} determined for each modeled channel to find a value of $\alpha_{CO} = 0.78 \pm 0.11$. As we could not model the red velocity component in SPT0538-50, for this galaxy we calculate α_{CO} for the blue velocity component only, yielding $\alpha_{CO} = 1.4 \pm 0.2$.

5.2.4. Summary of CO–H$_2$ Conversion Factor Measurements

We have constrained the CO–H$_2$ conversion factor in the two objects presented here using three independent methods. The three methods show reasonably good agreement with each other, with average values of $\alpha_{CO} = 1.3$ for SPT0346-52 and $\alpha_{CO} = 1.5$ for SPT0538-50. The uncertainty in these estimates is dominated by systematic, rather than statistical, errors of $\sim 100\%$ for each method. Given the large systematic uncertainties inherent to each method, the general agreement between the three techniques is encouraging. Resolved CO and dust continuum observations of a larger sample of objects
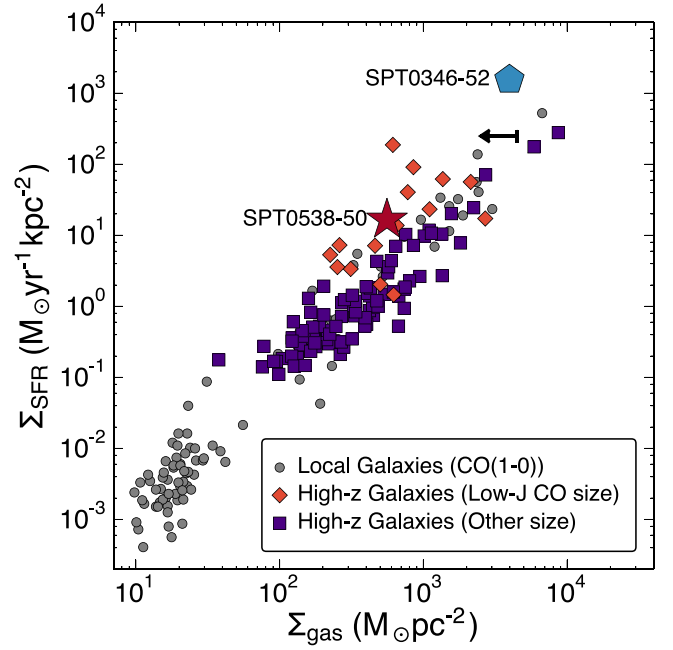

Figure 7. Schmidt–Kennicutt star formation relation. For all galaxies, we use CO–H$_2$ conversion factors using the Narayanan et al. (2012) formula. The high-redshift galaxies are separated into those that have been resolved in a low-J CO transition and those for which a higher line was observed (with a size determined from other means, generally the rest-frame optical/UV size). The black arrow shows the effect of the average correction to Σ_{gas} that results from the difference in size between the low-J CO emission and the rest-frame UV or dust emission, as seen in Figure 5. The local galaxy sample is from Kennicutt (1998), while the high-redshift sample is compiled from Younger et al. (2008), Genzel et al. (2010), Daddi et al. (2010), Ivison et al. (2011, 2013), Magdis et al. (2011), Fu et al. (2012, 2013), Hodge et al. (2012, 2015), Walter et al. (2012), and Tacconi et al. (2013).

could reveal systematic differences between the various methods.

For both objects, the derived conversion factors are similar to those determined for other rapidly star-forming objects, exhibiting low values of α_{CO} similar to most DSFGs and unlike more quiescently star-forming objects. In Figure 6, we place our measurements in the context of other studies that have also constrained the conversion factor in a wide variety of galaxies at $z > 1$. No clear bimodality between "Milky Way-like" and "ULIRG-like" values is seen, as would be expected from a heterogeneous collection of galaxies with varying ISM properties. Indeed, the sample used to determine the canonical "ULIRG-like" value of α_{CO} by Downes & Solomon (1998) also showed a fair amount of variation. This lack of bimodality (as noted by Narayanan et al. 2012 and discussed in the next section) can influence the form of the Schmidt–Kennicutt SF relation.

5.3. The SF Relation at z > 2.5

We now turn our attention to the Schmidt–Kennicutt Σ_{SFR}–Σ_{gas} relation. Figure 7 presents samples of low- and high-redshift galaxies for comparison to the targets of this work. Our lens modeling and FIR SED provide measurements of the total SFR, molecular gas mass (inferred from low-J CO measurements and the α_{CO} measurements of the previous section), and sizes of the star-forming and molecular gas regions. The Σ_{SFR} and Σ_{gas} values for these two objects show them to lie at the upper edge of the distribution of galaxies in this plane.

To interpret the offset between the properties of the SPT galaxies and the larger sample consisting of both normal and more highly star-forming galaxies, we must consider the measurements that are required to construct such a plot. The high-redshift comparison galaxies in Figure 7 are divided into two samples depending on whether their molecular gas sizes are determined from low-J CO (orange diamonds) or from other measurements, including SF tracers and higher-J CO (purple squares). The galaxies with low-J CO size measurements, which provide determinations of Σ_{gas} that are most similar to those made at low redshift, are more consistent with the SPT sources than the other high-redshift subsample. The typical procedure to convert from higher-J CO measurements to Σ_{gas} involves correcting the CO luminosity for subthermal excitation to arrive at the CO(1–0) equivalent, using α_{CO} to infer the molecular gas mass, and division by one of the available size measurements to get the surface density. However, in Section 5.1 we found that other measurements of galaxy size systematically underestimated the low-J CO size by a factor of $\sim$1.3, which corresponds to a $1.7\times$ underestimate in the area and overestimate in Σ_{gas}. This error is shown as a horizontal arrow in Figure 7, and is very similar to the offset seen between the two high-redshift galaxy samples. Clearly, care is needed when placing galaxies observed in heterogeneous ways on the SF relation. Further comprehensive studies of low-J CO emission by the VLA or ATCA offer the potential to resolve this issue by directly comparing the effective radii of high-redshift galaxies at various CO transitions.

6. CONCLUSIONS

We have presented spatially and spectrally resolved images of two gravitationally lensed dusty star-forming galaxies at redshifts $z = 2.78$ and $z = 5.66$. SPT0346-52 is among the most intrinsically luminous DSFGs, while the luminosity of SPT0538-50 is more typical of the DSFG population. Using a visibility-based lens modeling procedure, we have shown that SPT0346-52 has complex dynamics, and confirmed the merger hypothesis in SPT0538-50. By comparing with lens models derived from ALMA observations of the dust continuum in each galaxy, we find that the difference in magnification between the molecular gas and dust varies between 0 and 50%, mostly due to the larger physical extent of the gas compared to the area of active SF. In SPT0538-50, we have shown that the physical extent of the CO emission decreases with increasing transition, with the CO(3–2) emission being roughly the same size as the dust continuum. We have constrained the CO–H_2 conversion factor via three independent methods, finding values near those expected for highly star-forming systems. The three methods agree reasonably well when applied to these two objects; further in-depth studies may be able to discern systematic differences between the various methods. Finally, we have placed these two objects on the Schmidt–Kennicutt SF relation, finding that they lie along the upper envelope of vigorously star-forming systems. Part of this offset may be explained by the different effective source sizes of the CO emission as a function of observed transition, an effect that should be taken into account as larger samples of spatially resolved high-redshift molecular gas measurements become available.

REFERENCES

Abdo, A. A., Ackermann, M., Ajello, M., et al. 2010, ApJ, 710, 133
Aravena, M., Murphy, E. J., Aguirre, J. E., et al. 2013, MNRAS, 433, 498
Bigiel, F., & Blitz, L. 2012, ApJ, 756, 183
Blain, A. W., Moller, O., & Maller, A. H. 1999, MNRAS, 303, 423
Bolatto, A. D., Wolfire, M., & Leroy, A. K. 2013, ARA&A, 51, 207
Bothwell, M. S., Aguirre, J. E., Chapman, S. C., et al. 2013a, ApJ, 779, 67
Bothwell, M. S., Chapman, S. C., Tacconi, L., et al. 2010, MNRAS, 405, 219
Bothwell, M. S., Smail, I., Chapman, S. C., et al. 2013b, MNRAS, 429, 3047
Bussmann, R. S., Pérez-Fournon, I., Amber, S., et al. 2013, ApJ, 779, 25
Calanog, J. A., Fu, H., Cooray, A., et al. 2014, ApJ, 797, 138
Carilli, C. L., Daddi, E., Riechers, D., et al. 2010, ApJ, 714, 1407
Carilli, C. L., & Walter, F. 2013, ARA&A, 51, 105
Carlstrom, J. E., Ade, P. A. R., Aird, K. A., et al. 2011, PASP, 123, 568
Casey, C. M., Narayanan, D., & Cooray, A. 2014, PhR, 541, 45
Chabrier, G. 2003, PASP, 115, 763
da Cunha, E., Charlot, S., & Elbaz, D. 2008, MNRAS, 388, 1595
Daddi, E., Bournaud, F., Walter, F., et al. 2010, ApJ, 713, 686
Dale, D. A., Aniano, G., Engelbracht, C. W., et al. 2012, ApJ, 745, 95
Danielson, A. L. R., Swinbank, A. M., Smail, I., et al. 2011, MNRAS, 410, 1687
Deane, R. P., Heywood, I., Rawlings, S., & Marshall, P. J. 2013, MNRAS, 434, 23
Downes, D., & Solomon, P. M. 1998, ApJ, 507, 615
Draine, B. T., Aniano, G., Krause, O., et al. 2014, ApJ, 780, 172
Draine, B. T., & Li, A. 2007, ApJ, 657, 810
Dunne, L., Eales, S., Edmunds, M., et al. 2000, MNRAS, 315, 115
Dunne, L., & Eales, S. A. 2001, MNRAS, 327, 697
Engel, H., Tacconi, L. J., Davies, R. I., et al. 2010, ApJ, 724, 233
Faucher-Giguère, C.-A., Quataert, E., & Hopkins, P. F. 2013, MNRAS, 433, 1970
Förster Schreiber, N. M., Genzel, R., Bouché, N., et al. 2009, ApJ, 706, 1364
Fu, H., Cooray, A., Feruglio, C., et al. 2013, Natur, 498, 338
Fu, H., Jullo, E., Cooray, A., et al. 2012, arXiv:1202.1829
Genzel, R., Tacconi, L. J., Gracia-Carpio, J., et al. 2010, MNRAS, 407, 2091
Greve, T. R., Bertoldi, F., Smail, I., et al. 2005, MNRAS, 359, 1165
Greve, T. R., Vieira, J. D., Weiß, A., et al. 2012, ApJ, 756, 101
Harris, A. I., Baker, A. J., Frayer, D. T., et al. 2012, arXiv:1204.4706
Hayward, C. C., Jonsson, P., Kereš, D., et al. 2012, MNRAS, 424, 951
Hezaveh, Y. D., Marrone, D. P., Fassnacht, C. D., et al. 2013, ApJ, 767, 132
Hezaveh, Y. D., Marrone, D. P., & Holder, G. P. 2012, ApJ, 761, 20
Hinshaw, G., Larson, D., Komatsu, E., et al. 2013, ApJS, 208, 19
Hodge, J. A., Carilli, C. L., Walter, F., Daddi, E., & Riechers, D. 2013, ApJ, 776, 22
Hodge, J. A., Carilli, C. L., Walter, F., et al. 2012, ApJ, 760, 11

Hodge, J. A., Riechers, D., Decarli, R., et al. 2015, ApJL, 798, L18
Ivison, R. J., Papadopoulos, P. P., Smail, I., et al. 2011, MNRAS, 412, 1913
Ivison, R. J., Swinbank, A. M., Smail, I., et al. 2013, ApJ, 772, 137
James, A., Dunne, L., Eales, S., & Edmunds, M. G. 2002, MNRAS, 335, 753
Kennicutt, R. C., Jr. 1998, ApJ, 498, 541
Kennicutt, R. C., & Evans, N. J. 2012, ARA&A, 50, 531
Krumholz, M. R., McKee, C. F., & Tumlinson, J. 2009, ApJ, 699, 850
Leroy, A. K., Bolatto, A., Gordon, K., et al. 2011, ApJ, 737, 12
Leroy, A. K., Walter, F., Brinks, E., et al. 2008, AJ, 136, 2782
Leroy, A. K., Walter, F., Sandstrom, K., et al. 2013, AJ, 146, 19
Li, A., & Draine, B. T. 2001, ApJ, 554, 778
Liu, G., Koda, J., Calzetti, D., Fukuhara, M., & Momose, R. 2011, ApJ, 735, 63
Ma, J., Gonzalez, A. H., Spilker, J. S., et al. 2015, ApJ, in press
    (arXiv:1509.02835)
Magdis, G. E., Daddi, E., Béthermin, M., et al. 2012, ApJ, 760, 6
Magdis, G. E., Daddi, E., Elbaz, D., et al. 2011, ApJL, 740, L15
Magnelli, B., Saintonge, A., Lutz, D., et al. 2012, A&A, 548, A22
Messias, H., Dye, S., Nagar, N., et al. 2014, A&A, 568, A92
Mocanu, L. M., Crawford, T. M., Vieira, J. D., et al. 2013, ApJ, 779, 61
Narayanan, D., Dey, A., Hayward, C. C., et al. 2010, MNRAS, 407, 1701
Narayanan, D., & Krumholz, M. R. 2014, MNRAS, 442, 1411
Narayanan, D., Krumholz, M. R., Ostriker, E. C., & Hernquist, L. 2012,
    MNRAS, 421, 3127
Negrello, M., Hopwood, R., De Zotti, G., et al. 2010, Sci, 330, 800
Neri, R., Genzel, R., Ivison, R. J., et al. 2003, ApJL, 597, L113
Ossenkopf, V., & Henning, T. 1994, A&A, 291, 943
Rawle, T. D., Egami, E., Bussmann, R. S., et al. 2014, ApJ, 783, 59
Regan, M. W., Thornley, M. D., Helfer, T. T., et al. 2001, ApJ, 561, 218
Riechers, D. A., Cooray, A., Omont, A., et al. 2011, ApJL, 733, L12
Riechers, D. A., Walter, F., Brewer, B. J., et al. 2008, ApJ, 686, 851
Sakamoto, K., Aalto, S., Wilner, D. J., et al. 2009, ApJL, 700, L104
Sandstrom, K. M., Leroy, A. K., Walter, F., et al. 2013, ApJ, 777, 5
Schmidt, M. 1959, ApJ, 129, 243
Schruba, A., Leroy, A. K., Walter, F., et al. 2011, AJ, 142, 37
Scoville, N., Aussel, H., Sheth, K., et al. 2014, ApJ, 783, 84
Scoville, N. Z., Yun, M. S., & Bryant, P. M. 1997, ApJ, 484, 702
Serjeant, S. 2012, MNRAS, 424, 2429
Shetty, R., Kelly, B. C., & Bigiel, F. 2013, MNRAS, 430, 288
Solomon, P. M., Rivolo, A. R., Barrett, J., & Yahil, A. 1987, ApJ, 319, 730
Spilker, J. S., Marrone, D. P., Aguirre, J. E., et al. 2014, ApJ, 785, 149
Swinbank, A. M., Papadopoulos, P. P., Cox, P., et al. 2011, ApJ, 742, 11
Swinbank, A. M., Smail, I., Longmore, S., et al. 2010, Natur, 464, 733
Tacconi, L. J., Genzel, R., Smail, I., et al. 2008, ApJ, 680, 246
Tacconi, L. J., Neri, R., Genzel, R., et al. 2013, ApJ, 768, 74
Thompson, T. A., Quataert, E., & Murray, N. 2005, ApJ, 630, 167
Thomson, A. P., Ivison, R. J., Owen, F. N., et al. 2015, MNRAS, 448, 1874
Vieira, J. D., Crawford, T. M., Switzer, E. R., et al. 2010, ApJ, 719, 763
Vieira, J. D., Marrone, D. P., Chapman, S. C., et al. 2013, Natur, 495, 344
Walter, F., Decarli, R., Carilli, C., et al. 2012, Natur, 486, 233
Wardlow, J. L., Cooray, A., De Bernardis, F., et al. 2013, ApJ, 762, 59
Weiß, A., De Breuck, C., Marrone, D. P., et al. 2013, ApJ, 767, 88
Wilson, C. D., Warren, B. E., Israel, F. P., et al. 2009, ApJ, 693, 1736
Younger, J. D., Fazio, G. G., Wilner, D. J., et al. 2008, ApJ, 688, 59
Zahid, H. J., Dima, G. I., Kudritzki, R.-P., et al. 2014, ApJ, 791, 130